

Fluorescence-enhanced optical imaging in large tissue volumes using a gain-modulated ICCD camera

Anuradha Godavarty¹, Margaret J Eppstein², Chaoyang Zhang²,
Sangeeta Theru¹, Alan B Thompson¹, Michael Gurfinkel¹
and Eva M Sevick-Muraca^{1,3}

¹ Department of Chemical Engineering, Texas A&M University, College Station,
TX 77843-3122, USA

² Department of Computer Science, University of Vermont, Burlington, VT 05405, USA

Received 22 November 2002, in final form 3 April 2003

Published 3 June 2003

Online at stacks.iop.org/PMB/48/1701

Abstract

A novel image-intensified charge-coupled device (ICCD) imaging system has been developed to perform 3D fluorescence tomographic imaging in the frequency-domain using near-infrared contrast agents. The imager is unique since it (i) employs a large tissue-mimicking phantom, which is shaped and sized to resemble a female breast and part of the extended chest-wall region, and (ii) enables rapid data acquisition in the frequency-domain by using a gain-modulated ICCD camera. Diffusion model predictions are compared to experimental measurements using two different referencing schemes under two different experimental conditions of perfect and imperfect uptake of fluorescent agent into a target. From these experimental measurements, three-dimensional images of fluorescent absorption were reconstructed using a computationally efficient variant of the approximate extended Kalman filter algorithm. The current work represents the first time that 3D fluorescence-enhanced optical tomographic reconstructions have been achieved from experimental measurements of the time-dependent light propagation on a clinically relevant breast-shaped tissue phantom using a gain-modulated ICCD camera.

 This article features online multimedia enhancements

(Some figures in this article are in colour only in the electronic version)

³ Author to whom correspondence should be addressed. The Photon Migration Laboratories, Texas A&M University, College Station, TX 77843-3573, USA.

1. Introduction

Over the past five years, several laboratories have embarked on the development of fluorescence-enhanced optical imaging as a new modality for molecularly based, diagnostic imaging in deep tissues, particularly in the female breast (Sevick-Muraca *et al* 2003). Unlike near-infrared (NIR) optical imaging where endogenous contrast in tissue optical properties differentiates normal from diseased tissues, fluorescence-enhanced optical imaging uses molecularly targeting exogenous fluorescent agents to enhance the optical contrast with specificity for disease. As listed in table 1, various investigators have demonstrated fluorescence-enhanced optical tomography using continuous wave (CW), time-domain photon migration (TDPM), or frequency-domain photon migration (FDPM) measurements (O'Leary *et al* 1994, 1996, Wu *et al* 1995, 1997, Chang *et al* 1995, 1997, 1998, Paithankar *et al* 1997, Jiang 1998, Hull *et al* 1998, Eppstein *et al* 1999a, 1999b, 2002, Chernomordik *et al* 1999, Roy and Sevick-Muraca 1999, 2000, 2001a, 2001b, Yang *et al* 2001, Hawrysz *et al* 2001, Ntziachristos and Weissleder 2001, Lee and Sevick-Muraca 2002). Of all these studies, only a few employ actual experimental data to reconstruct three-dimensional images (Chernomordik *et al* 1999, Yang *et al* 2001, Hawrysz *et al* 2001, Ntziachristos and Weissleder 2001, Lee and Sevick-Muraca 2002, Eppstein *et al* 2002). Furthermore, the experimental studies with 3D reconstructions performed to date are limited either to (i) smaller volume phantom models ($<100\text{ cm}^3$) or *in vivo* studies on small rodent models of clinically irrelevant volumes (Yang *et al* 2001, Ntziachristos and Weissleder 2001) or (ii) compressed tissue-mimicking phantom geometries of large volumes ($\sim 260\text{ cm}^3$) (Eppstein *et al* 2002, Hawrysz *et al* 2001, Lee and Sevick-Muraca 2002), where information at the nipple region and the chest wall may be lost. In addition these previous studies involve slow and laborious data acquisition and calibration procedures owing to single source–detector detection schemes that employ multiplexed or individual detectors (Eppstein *et al* 2002, Hawrysz *et al* 2001, Lee and Sevick-Muraca 2002), although recently a CCD scanner was used by Ntziachristos and Weissleder (2002) for rapid acquisition of CW measurements in order to reconstruct images of small cylindrical volumes ($\sim 74\text{ cm}^3$) containing a rodent. However, to date, there remains a need for a time-dependent fluorescence imaging measurement approach, which can interrogate large volumes that mimic female breast geometries with appropriately fast data acquisitions while maintaining sufficient signal to noise for 3D tomographic reconstructions. In general, time-dependent measurement techniques such as frequency- and time-domains tend to provide an enhanced optical contrast over time-independent continuous-wave imaging techniques (Houston *et al* 2003, Delpy and Cope 1997). In this contribution, tomographic reconstructions are presented from three-dimensional FDPM measurements obtained on the surface of a large phantom ($\sim 1087\text{ cm}^3$) mimicking the female breast geometry. Data acquisition with a gain-modulated ICCD camera enables rapid and simultaneous data acquisition of light propagation between a source fibre, providing point illumination of excitation light, and multiple collection fibres enabling point collection of multiply scattered excitation and fluorescent light at numerous positions across the surface of the phantom.

In the following, we describe the breast-shaped tissue-mimicking phantom, the instrumentation associated with the novel FDPM ICCD imaging system, and the referencing schemes employed on the measurements. Comparisons of the experimental FDPM measurements with predictions from a finite element forward model of the coupled diffusion equations of excitation and fluorescently emitted light illustrate the accuracy of the forward model. Preliminary 3D reconstructions obtained using a computationally efficient variant of the approximate extended Kalman filter (AEKF) algorithm establish the feasibility of 3D

Table 1. Fluorescence-enhanced contrast imaging: literature of image reconstructions.

References	Inversion formulation	Data type	Noise	2D or 3D	Forward method	Measurement method	Contrast agent	Uptake ratio
O'Leary <i>et al</i> (1994)	Localization	Expt Phantom	Yes	2D	None	TDPM	ICG	Perfect uptake
Wu <i>et al</i> (1995)	Localization	Expt Phantom	Yes	3D	None	TDPM	Diethylthiatricarbocyanine	Perfect uptake
Chang <i>et al</i> (1995)	POCS, CGD, SART	Expt phantom	Yes	2D	NS	CW	Rhodamine 6G dye	Perfect uptake & 1000:1
O'Leary <i>et al</i> (1996)	SIRT	Synthetic data	0.1° in phase, 1% in amplitude	2D	Analytical	FDPM	ICG	Perfect uptake, 20:1
Paithankar <i>et al</i> (1997)	Newton–Raphson	Synthetic data	0.1°–1° in phase; 0.01 in log ac (Gaussian)	2D	MFD	FDPM	ICG	20:1
Wu <i>et al</i> (1997)	Laplace transform	Expt phantom	Yes	2D	NS	TDPM	HITCI iodide dye	Perfect uptake
Chang <i>et al</i> (1997)	POCS, CGD, SART	Expt phantom	Yes	2D	NS	CW	Rhodamine 6G dye	500:1
Chang <i>et al</i> (1998)	Conjugate gradient	Synthetic data	1–10% white noise	2D or 3D	NS	CW/ FDPM	N/A	100:1
Jiang (1998)	Newton's iterative method	Synthetic data	0–5%	2D	FEM	FDPM	N/A	2:1 contrast in ϕ , τ
Hull <i>et al</i> (1998)	Localization	Expt phantom	Yes	2D	Monte Carlo	CW	Nile Blue A	Perfect uptake
Eppstein <i>et al</i> (1999a, 1999b)	AEKF	Synthetic data	0.1° in phase; 1% in log ac (Gaussian)	2D, 3D	MFD	FDPM	N/A	Perfect uptake & 100:1 10:1, contrast in ϕ , τ , μ_a
Chernomordik <i>et al</i> (1999)	Random walk theory	Expt phantom	Yes	2D & 3D	NS	CW	Rhodamine	Perfect uptake
Roy and Sevick-Muraca (1999, 2000)	Gradient-based & truncated Newton method	Synthetic data	0.1° in phase; 1% in log ac (Gaussian)	2D	FEM	FDPM	N/A	2.5:1 5:1 10:1
Yang Y <i>et al</i> (2000)	Marquardt & Tikhonov regularization	<i>In vivo</i> (rats)	Yes	2D images	FEM	FDPM	ICG & DTTCI	Perfect & Imperfect uptake
Eppstein <i>et al</i> (2002), Hawrysz <i>et al</i> (2001)	AEKF	Expt phantom	Yes	3D	MFD	FDPM	ICG	50:1 100:1
Roy and Sevick-Muraca (2001a, 2001b)	Gradient-based optimization & truncated Newton's method	Synthetic data	55 dB in excitation; 35 dB in emission	2D, 3D	FEM	FDPM	N/A	10:1

Table 1. (Continued.)

References	Inversion formulation	Data type	Noise	2D or 3D	Forward method	Measurement method	Contrast agent	Uptake ratio
Ntziachristos <i>et al</i> (2001)	SIRT	Expt phantom	2% amplitude noise in source	2D along z-planes	FD	CW	ICG in background; Cy5.5 as contrast tumour	Perfect uptake
Lee and Sevick-Muraca (2002)	Levenberg–Marquardt	Expt phantom	Yes	3D	MFD	FDPM	ICG	100:1

CGD: conjugate gradient descent, CW: continuous-wave imaging, Expt: experimental, FD: finite difference, FDPM: frequency-domain photon migration, FEM: finite element method, MFD: multi-grid finite difference, N/A: not applicable, NS: not specified, POCS: projection onto convex sets, SART/SIRT: simultaneous algebraic reconstruction techniques, TDPM: time-domain photon migration, ϕ , τ : quantum efficiency and lifetime of the contrast agent.

tomographic imaging. Future work required for translating FDPM fluorescence-enhanced imaging into the clinic is briefly discussed.

2. Method and materials

2.1. Phantom model

The phantom model, made of PVC, was constructed to mimic the geometry of a breast and its surrounding chest-wall regions. Figure 1 shows the 3D cup-shaped model consisting of a hemispherical portion (10 cm inner diameter and 0.5 cm wall thickness) representing the breast tissue geometry, and a cylindrical portion (20 cm inner diameter, 10 cm height and 0.5 cm wall thickness) representing the extended chest-wall region and the underlying tissues around the breast.

Multimode optical fibres (model FT-1.0-EMT, Thorlabs Inc., NJ) of 1000 μm diameter and numerical aperture (NA) of 0.39 were used to illuminate and collect excitation and emission light. A total of 27 source and 128 collector fibres were symmetrically placed along alternate concentric rings on the hemispherical portion of the phantom in order to illuminate and collect the light signal from the phantom surface. In the current experimental studies, the phantom volume considered was 1087 cm^3 (i.e. up to 2.5 cm of the 10 cm height of the cylindrical portion of the model was considered for experiments).

Unlike studies involving phantom geometries mimicking a compressed breast or conical-shaped tissues (Eppstein *et al* 2002, Hawrysz *et al* 2001, Lee and Sevick-Muraca 2002, Hebden *et al* 2001), the use of the cup-shaped phantom will enable assessment of imaging information around the nipple and chest-wall regions.

2.2. Instrumentation

Modulated light (783 nm) from a high power laser diode (HPD1105-9mm-D-78505 model, High Power Devices Inc., NJ), which was mounted on a customized laser mount (model TCLDM9), was launched onto the phantom surface using the multimode optical fibres (source fibre) that were SMA coupled at the laser end. Modulation was accomplished by superimposing a 100 MHz ac signal of +30 dBm RF power onto the constant dc bias from the laser diode.

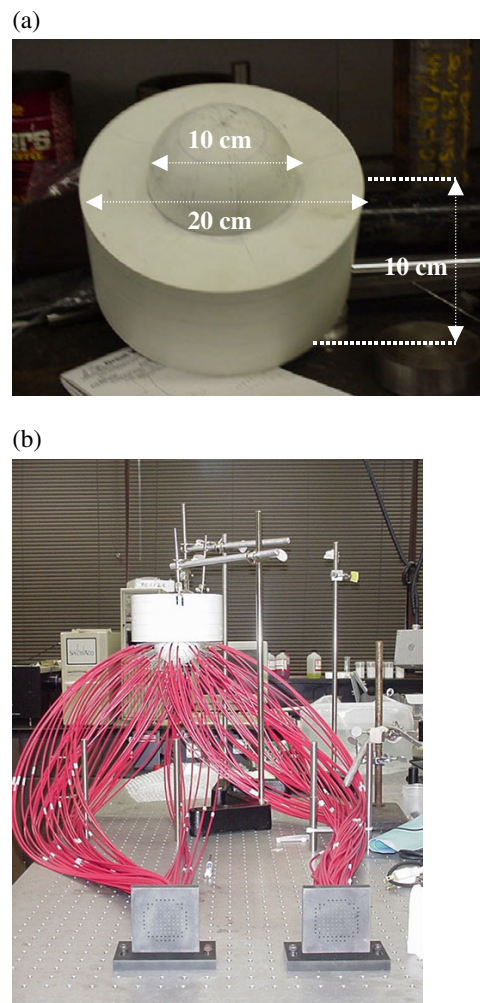


Figure 1. 3D tissue-mimicking phantom. (a) Inner dimensions of the breast-shaped hollow phantom shell. (b) The phantom shell was inverted and filled with 1% Liposyn solution with a suspended fluorescent target. Fibre optic collection on the cup was mounted to the interfacing plates for detection.

In order to obtain the +30 dBm ac signal, RF power of -7 dBm that was generated by a frequency synthesizer (Marconi Instruments model 2022 D, UK) was amplified using a +37 dBm amplifier (ENI-403LA model, Rochester). Hence, the laser diode delivered ~ 157 mW of optical power to each of the source fibres sequentially.

In this study, the technique of area detection was employed to overcome the slow and laborious data acquisition rate or replication of hardware associated with individual photon multiplier tubes (PMTs) or photodetectors. Here, the collection fibres from the phantom surface were arranged as 2D arrays on two black nylon interfacing plates (see figure 1), which were in turn imaged onto the photocathode of the image intensifier. The interfacing plates, each holding 64 collector fibres, were imaged over a diameter of 5 cm at both the excitation and emission wavelengths (resolution of 128×128 pixels) using the ICCD detection system.

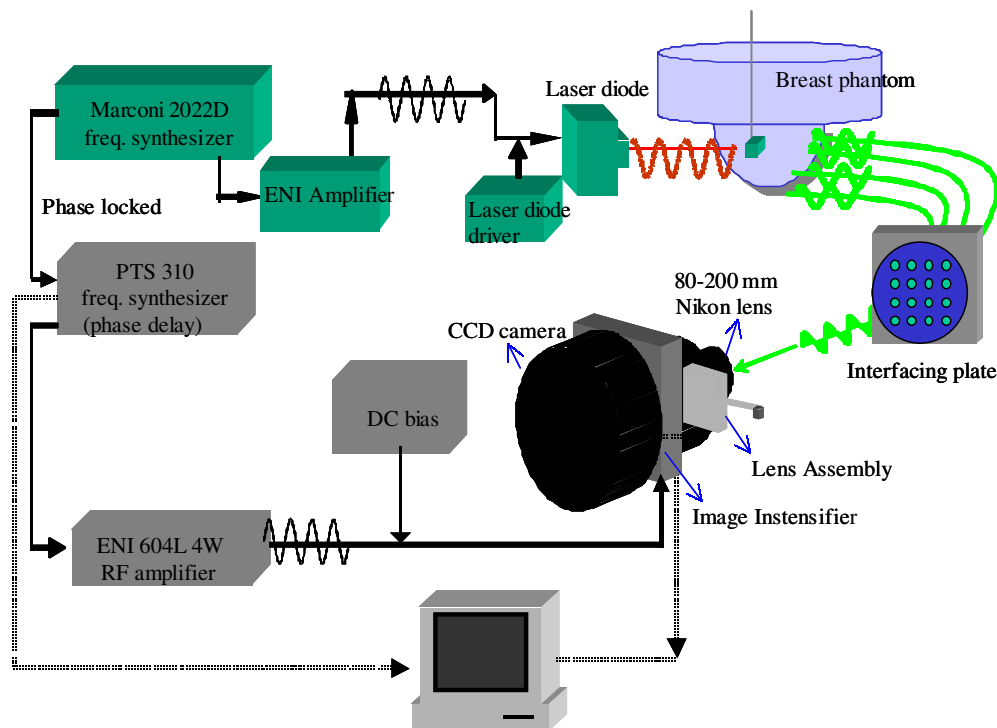


Figure 2. Instrumentation of the homodyne ICCD imaging system.

Figure 2 provides a schematic of the instrumentation of the homodyned ICCD imaging system. The major components of this detection system include: (i) a thermoelectrically cooled 12-bit CCD camera (TE/CCD-512-EFT Photometric CH12, Roper Scientific, NJ); (ii) a gain-modulated image intensifier (FS9910C Gen III model, ITT Night Vision, VA) and (iii) oscillators (or frequency synthesizers) that sinusoidally modulate the image intensifier and the laser diode. The gain-modulated image intensifier consists of a photocathode (operated at -65 V), multi-channel plate (MCP) (operated at 0 – 1000 V adjustable) and a phosphor screen (operated at 4000 V). The photocathode is coupled to a variable focal length Nikon lens (80 – 200 mm $f/2.8D$ AF-S model, Nikon, NY) in order to focus the detected image from the interfacing plate onto the photocathode, and the phosphor screen end of the image intensifier is optically coupled to the CCD camera. The photocathode of the image intensifier is modulated at 100 MHz using a PTS-310 frequency synthesizer (Programmed Test Sources model 10M201GYX-53, Littleton, MA), which delivers $+13$ dBm of RF power (Lakowicz and Berndt 1991, Reynolds *et al* 1997, Thompson and Sevic-Muraca 2003). This RF signal is further amplified to $+40$ dBm using an external amplifier (ENI model 604L-01, Rochester, NY). A constant dc voltage from a GBS micro power supply (model PS20060500, San Jose, CA) is superimposed onto the ac signal provided to the photocathode of the image intensifier. The system is operated in homodyne mode, since both the laser diode (at the source end) and the image intensifier (at the detector end) are modulated at the same frequency of 100 MHz. The oscillators driving the laser diode and the photocathode of the image intensifier are phase locked with a reference phase of 10 MHz in order to operate the system at a set and known phase difference.

A lens assembly housing suitable filters such as holographic filters, interference filters and neutral density filters is placed between the 80–200 mm Nikon lens and the image intensifier in order to obtain emission and excitation measurements at 830 nm and 785 nm wavelengths, respectively. The weak fluorescent signal is acquired using a combination of (i) holographic notch filter (HNPF-785.0-2.0 model, Kaiser Optical Systems Inc., Ann Arbor, MI) of 785 nm centre wavelength and <20 nm bandwidth, and (ii) an 830 nm interference filter (F10-830.0-4-2.0 model, CVI Laser Corp., NM) of 831 nm centre wavelength, 10 nm bandwidth and a blocking optical density (OD) of 4.0. This filter combination helps minimize the excitation light leakage as well as reject light outside the bandwidth of the emission wavelength (Houston *et al* 2003). Neutral density filters (Newport Corp., CA) of varying OD are used to attenuate the strong excitation signal collected from the phantom surface, and hence prevent damage to the image intensifier.

Data at excitation and emission wavelengths were acquired from both the interfacing plates by illuminating the phantom with individual point sources. A phase delay was introduced between the oscillators of the laser diode and the image intensifier and steady-state images were obtained at phase delays varying from 0 to 2π . In this work, a total of five such steady-state images (i.e. five repetitions) were acquired at 32 phase delays with integration times varying between 0.2 and 1 s in the CCD camera. Repetitions were performed in order to obtain an explicit estimate of the measurement error of the imaging system for use in the image reconstruction algorithm (see sections 2.6 and 3.1 for more details). The images acquired over a complete cycle of 0 to 2π were used to extract the amplitude and phase shift of the 128×128 -pixelated image employing fast Fourier transforms (FFT). Previous work using a similar homodyne ICCD camera in a multipixel system, involving area illumination and area detection has been demonstrated in phantom studies (Reynolds *et al* 1997, Thompson *et al* 2003) and *in vivo* studies using canine animal models (Reynolds *et al* 1999, Gurfinkel *et al* 2000).

2.3. Experimental parameters and data acquisition

Experiments were performed under conditions of imperfect uptake (100 : 1) and perfect uptake (1 : 0) of 1 μM ICG in the 1 cm^3 target. The target was a hollow clear acrylic cube of $1 \times 1 \times 1 \text{ cm}^3$ that was filled with varying concentrations of ICG in 1% Liposyn solution, such that it provided optical contrast with respect to the background. The target was suspended $\sim 1 \text{ cm}$ deep from the hemispherical surface of the phantom at $(-2.5, -0.5, 2.5) \text{ cm}$ (from the centre of the circular base of the hemispherical portion of the phantom), using two 1 mm optical fibres for support. A plastic lid with 1 mm drilled holes on its x - y plane facilitated the positioning of the target accurately in the 1% Liposyn phantom. The optical properties of the fluorophore-free background fluid (1% Liposyn solution, Abbott Laboratories, North Chicago, IL) filling the hollow cup-shaped phantom were characterized from single-pixel FDPM measurements in terms of their absorption and scattering coefficients at excitation and emission wavelengths (Sun *et al* 2002). The optical properties of the fluorescing agent were determined using the following relation:

$$\mu_{ax,mf} = 2.3 \times \varepsilon_{ax,m} \times C \quad (1)$$

where, $\mu_{ax,mf}$ is the absorption coefficient due to the fluorescing agent (suffix 'f') at the excitation (suffix 'x') and emission wavelengths (suffix 'm'), respectively, $\varepsilon_{ax,m}$ is the extinction coefficient at the excitation and emission wavelengths, respectively ($\varepsilon_{ax} = 130\,000 \text{ M}^{-1} \text{ cm}^{-1}$, $\varepsilon_{am} = 11\,000 \text{ M}^{-1} \text{ cm}^{-1}$) and C is the concentration of the fluorescing agent (mol l^{-1}).

Table 2 lists the optical properties of the background and target, consisting of 1% Liposyn solution and the appropriate concentrations of ICG for both the perfect and imperfect uptake

Table 2. Optical properties of background and target in the perfect uptake and imperfect uptake experiments.

Optical properties (cm ⁻¹)		Perfect uptake (1:0)		Imperfect uptake (100:1)	
		Target	Background	Target	Background
Excitation	$\mu_{axf} + \mu_{axi}$	0.300 + 0.023	0.00 + 0.023	0.300 + 0.023	0.0030 + 0.023
	μ_{sx}	10.18	10.18	10.18	10.18
Emission	$\mu_{amf} + \mu_{ami}$	0.025 + 0.031	0.00 + 0.031	0.025 + 0.031	0.000 25 + 0.031
	μ_{sm}	8.64	8.64	8.64	8.64

μ_{axf} , μ_{amf} : Absorption coefficient due to the fluorophores at excitation and emission wavelengths, respectively.

μ_{axi} , μ_{ami} : Absorption coefficient due to the chromophores at excitation and emission wavelengths, respectively.

conditions. Data acquisition was initiated after minimizing the dark current noise of the CCD camera. ICCD images of all 64 fibre collection points on each interfacing plate were acquired only for source locations (arbitrarily selected in the general region of interest) where the average emission signal on the corresponding plate was above the noise floor (i.e., the modulation depth (ac/dc) was at least 0.1). Sources farther from the target that were tested did not meet the above criterion and hence data were not acquired for these source locations. The positioning of the collection fibres on the two plates was mapped onto the 128 × 128 pixels of the CCD camera and the amplitude and phase shift information of each collection fibre point was extracted at both the wavelengths. A total of 768 measurements (using seven sources) and 512 measurements (using six sources) were acquired at each of the excitation and emission wavelengths in the imperfect and perfect uptake experiments, respectively.

The total data acquisition time for each experimental case was a function of (i) exposure time of the camera (varying between 0.2 and 1 s), (ii) number of measurement repetitions performed (five in our case), (iii) number of interfacing plates imaged (i.e. one or two) and (iv) number of sources used to acquire fluorescence measurements (varying between 1 and 27). On an average, the data acquisition time for the fluorescent signal was approximately 35 min for all five repetitions in each experimental case. In comparison to our earlier system using photon multiplier tubes (PMTs) for detecting single source–detector pair sequentially (Eppstein *et al* 2002), the current system imaging multiple source–detector pairs is at least 4–7 times faster (based on the exposure time set on the CCD camera). The data acquisition time could further be reduced by optimally designing a single interfacing plate to hold all the 128 collection fibres without compensating the resolution of the images, and also by using faster CCD cameras of current generation.

2.4. Data referencing schemes

Two different referencing schemes were evaluated for their effectiveness in accounting for instrument effects and the unknown source strength. The first scheme considered the fluence data obtained at emission wavelength, Φ_m , relative to the fluence data obtained at excitation wavelength, Φ_x , at each collection fibre location (Lee and Sevick-Muraca 2002, Roy *et al* 2003)

$$\frac{(\Phi_m)_i}{(\Phi_x)_i} \quad i = \text{collection fibres } 1, \dots, n \quad (2)$$

where $\Phi_{x,m} = I_{acx,m} \exp(i\theta_{x,m})$, and the subscripts x and m correspond to excitation and emission wavelengths, respectively. Thus, the relative phase shift (RPS, $\Delta\theta = \theta_m - \theta_x$) and

ac ratio ($ACR = I_{ac,m}/I_{ac,x}$) were computed accordingly from the measurements obtained at all the collection fibres, in response to illumination from each of the source fibres. Prior work by Lee and Sevick-Muraca (2002) and Roy *et al* (2003) indicated that use of the referencing scheme given by equation (2) is computationally advantageous in the inversion algorithm. Additionally, referencing emission by excitation wavelength individually for each detector has the advantage that any discrepancies in optical fibre length are automatically accounted for. However, in order to employ the above referencing scheme, the wavelength-dependent responses of the image intensifier and filters need to be accounted for. It was assumed that the RPS remained independent of wavelength and that the varying wavelengths impacted only the ACR. Hence a wavelength-dependent factor (F) was evaluated in order to account for wavelength effects due to different filters (neutral density, interference and holographic filters) and image intensifier, and also for the differing integration times set on the CCD camera. The factor to account for wavelength dependence is computed as

$$F = \left(\frac{T_x^{-OD}}{T_m^{-OD}} \right)_{ND} \times \left(\frac{t_x}{t_m} \right) \times \left(\frac{1}{T_{\text{holographic}}} \right) \times \left(\frac{1}{T_{830\text{-interference}}} \right) \times \left(\frac{QE_x}{QE_m} \right)_{II} \quad (3)$$

where, the subscripts x and m correspond to the excitation and emission wavelengths, respectively; T is the transmission of the respective filters such as neutral density (ND), holographic or 830 nm interference filter. OD represents the actual optical density of the ND filters at the corresponding wavelengths; t is the integration time (or exposure time) of the CCD camera at either wavelengths and QE is the quantum efficiency of the image intensifier (II). The true ACR was determined by multiplying the experimentally obtained ACR with the factor F , given in equation (3).

A second referencing scheme that was employed in our earlier studies (Eppstein *et al* 2002, Hawrysz *et al* 2001, Lee and Sevick-Muraca 2002) was also evaluated. Here, the emission fluence data from multiple collection fibre locations were referenced with respect to the emission fluence data from a single specified reference collection fibre (ref), as shown in equation (4)

$$\frac{(\Phi_m)_i}{(\Phi_m)_{\text{ref}}} \quad (4)$$

Here, the RPS and ACR are given by $\Delta\theta = \theta_m - \theta_{m,\text{ref}}$ and $I_{ac,m}/I_{ac,m,\text{ref}}$, respectively. Good results were achieved when reference fibres were selected, for each source and for each interfacing plate, as the fibre at that location was at least 2 cm away from the point of illumination. In this referencing scheme, variations in collection fibre lengths should be explicitly accounted for, since fibre length impacts the measured phase shift.

2.5. Forward model

The coupled diffusion equations describing light propagation and fluorescence generation in a turbid medium were solved in Matlab V. 6.1 using the Galerkin approximation of the finite element method (FEM) along with the partial current boundary condition (Zeinkiewicz and Taylor 1989, Reddy 1993). The refractive index mismatch parameter in the partial current boundary condition was set to 0.0222 for Liposyn/PVC boundaries and 0.431 for the air/Liposyn boundary (Godavarty *et al* 2002, Haskell *et al* 1994) using refractive index values of 1.33, 1.5 and 1.0 for Liposyn solution, PVC and air, respectively. The FEM mesh consisted of 6956 nodes and 34 413 tetrahedral elements (figure 3(a)). In the hemispherical portion of the mesh, the average node spacing was 0.5 cm, and the average element volume was 0.013 cm³. Computational efficiency of the forward solver was improved by employing a high degree of vectorization in the code, often at the expense of added memory requirements

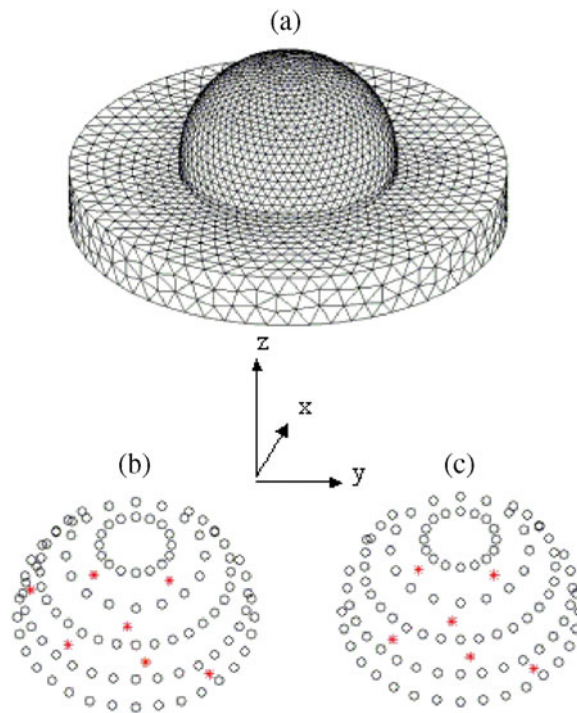


Figure 3. (a) Surface view of the finite element mesh used for the forward and inverse models. (b) Locations of sources (asterisks) and detectors (circles) for the imperfect uptake experiments. (c) Locations of sources and detectors for the perfect uptake experiments.

(Fedele *et al* 2003). For the mesh shown in figure 3(a), 4 s of CPU time was required on a 2.2 GHz Pentium IV to assemble the global finite element matrices. An additional 5 s of CPU time was required to solve for the complex fluence at excitation and emission wavelengths for each separate point source illumination. The fluence data obtained at both the wavelengths for each source–detector pair were then referenced using one of the two referencing schemes (equation (2) or (4)). By comparing model predictions (obtained by employing known spatial optical properties in the forward model) to experimental measurements, the ‘model error’ (defined as the difference between measurements and simulations from forward model) was assessed for all the source–detector pairs (section 3.1). Although finer meshes gave lower model error, the above mesh was used for image reconstructions in order to optimize computational costs at the expense of added discretization error.

2.6. Image reconstruction algorithm

Three-dimensional image reconstructions were performed using a variant of the Bayesian approximate extended Kalman filter (AEKF) algorithm (Eppstein and Dougherty 1996). The AEKF is a stochastic method based on the statistically stronger criterion of minimizing the variance of the parameter error, given estimates of measurement, model and initial parameter estimation errors, rather than simply minimizing the output error. It offers several advantages for inverting low SNR data, including (i) physically based weighting of parameter updates that explicitly accounts for spatially variant measurement and model error covariances (\mathbf{R} and \mathbf{Q} , respectively), (ii) co-estimation of the spatially variant parameter error covariance (\mathbf{P}) that

can be used as a measure of final parameter uncertainty and (iii) enhanced convergence by damping on the inverse of the evolving parameter error covariance. Prior studies with the AEKF have verified that use of actual spatially variant measurement errors and recursively updated parameter errors increases the accuracy and stability of reconstructions of fluorescence absorption from noisy data (Eppstein *et al* 2002).

In this work, a computationally efficient variant of the AEKF was applied, as shown in the following pseudo-code:

```

iterate
  1 :  $\mathbf{x} = f(\mathbf{y})$ 
  for  $i = 1$  to #sources
    2 :  $\mathbf{J}_i = \frac{\partial \mathbf{x}_i}{\partial \mathbf{y}}$ 
    3 :  $\mathbf{K}_i = \mathbf{P} \cdot \mathbf{J}_i^T \cdot (\mathbf{R}_i + \mathbf{Q}_i + \mathbf{J}_i \cdot \mathbf{P} \cdot \mathbf{J}_i^T)^{-1}$ 
    4 :  $\Delta \mathbf{y}_i = \mathbf{K}_i \cdot (\mathbf{z}_i - \mathbf{x}_i)$ 
    5 :  $\mathbf{P} \leftarrow full(diag(\mathbf{P} - \mathbf{K}_i \cdot \mathbf{J}_i \cdot \mathbf{P}))$ 
  end
  6 :  $\mathbf{y} \leftarrow \mathbf{y} + \sum_i \Delta \mathbf{y}_i$ 
until convergence.

```

Here, \mathbf{x} represents distributed predictions of the measurable state variables (ln(ACR) and RPS) using the forward simulator f described in section 2.5 with the current estimates of uncertain optical parameters \mathbf{y} . Since the algorithm assumes a normal distribution of errors, we transform fluorescence absorption (μ_{axf}) to a normally distributed random variable using a pseudo-beta transform (Eppstein *et al* 1999b), assuming that μ_{axf} is beta-distributed with lower and upper bounds of 0.0 cm^{-1} and 0.8 cm^{-1} , respectively. In these experiments, the parameter vector \mathbf{y} contains evolving estimates of transformed fluorescence absorption in the hemispherical portion of the domain; the resulting retransformed absorption estimates are thus constrained to the feasible range (Eppstein *et al* 1999b). Fluorescence absorption at the emission wavelength (μ_{amf}) is linearly related to fluorescence absorption at the excitation wavelength (μ_{axf}) by the factor $\varepsilon_{am}/\varepsilon_{ax} = 0.0846$, since absorption at each wavelength is governed by equation (1), thus enabling the co-estimation of μ_{amf} from μ_{axf} . While the outer loop represents iterations over the entire batch of data, the inner loop represents sequential incorporation of data by source, where subscript i refers to the portion of each matrix or vector corresponding to measurements from source i . In the inner loop, the Jacobian for source i (\mathbf{J}_i) is calculated with the adjoint approach (Fedele *et al* 2003) and is used to compute a weighted, damped nonlinear least-squares parameter update based on discrepancies between measurements (\mathbf{z}_i) and predictions (\mathbf{x}_i) for the particular source. The inverse of the sum of the measurement and model error covariances $(\mathbf{R}_i + \mathbf{Q}_i)^{-1}$ is used to weight the updates and the inverse of the evolving parameter error covariance (\mathbf{P}^{-1}) is used to damp the updates (statement 3 of the pseudo-code). For computational efficiency, parameter errors are assumed to remain uncorrelated (Eppstein *et al* 2002), and consequently only the diagonal elements of the covariance \mathbf{P} are stored and recursively updated after processing data from each source (statement 5 of the pseudo-code). The inversion algorithm used here differs slightly from the AEKF as reported previously (Eppstein *et al* 1999a, 1999b, 2002) in that the actual update of the parameters \mathbf{y} (statement 6 of the pseudo-code), and consequent re-prediction of \mathbf{x} (statement 1 of the pseudo-code) have been moved to an outer loop and are not executed every time the parameter error variance is updated (statement 5 of the pseudo-code). This

variant of the AEKF is more computationally efficient and preliminary studies indicate that it gives results that are at least as accurate as the original AEKF algorithm (Zhang *et al* 2003). Furthermore, while data-driven zonation has been shown to improve accuracy and stability on inversions in 2D (Eppstein *et al* 1999a) and 3D (Eppstein *et al* 2002) rectangular domains, it was not found to be the case for the current breast-shaped phantom. Work is in progress to determine the possible reasons and also explore the numerical effects of data-driven zonation. The zonation technique has, however, not been employed for the results presented here.

The measurement error covariance \mathbf{R} was estimated as a diagonal matrix from the variances of the means of five measurement repetitions from each individual source–detector fibre pair, so each \mathbf{R}_i is spatially variant and distinct. Unlike the unbiased portion of the measurement error variance, it is not possible to accurately determine the model error covariance \mathbf{Q} for unknown domains. In a previous work (Eppstein *et al* 2002), the model error variance was approximated to be spatially invariant based on the average estimates of model error variance of both $\ln(\text{ACR})$ and RPS, where the model error variance of both $\ln(\text{ACR})$ and RPS was determined by comparing measurements with predictions from the forward model on several known phantoms. In the current work, the model error variance was approximated to be spatially variant by scaling the inverse of the modulation depth (i.e. dc/ac) for $\ln(\text{ACR})$ and for RPS, in accordance with ranges of model errors observed on these and other datasets, so each \mathbf{Q}_i is also spatially variant and distinct. Initial parameter error variance was empirically set to 0.1. The reconstructions were terminated when either the sum of squared prediction error was reduced by less than 1% or when 50 iterations had been reached.

3. Results and discussion

3.1. Model prediction error

As stated in section 2.3, data from a total of 5 repetitions of FDPDM measurements were acquired at each of 768 source–detector pairs in the imperfect uptake experiment (figure 3(b)), and at each of 512 source–detector pairs in the perfect uptake experiment (figure 3(c)). The means of $\ln(\text{ACR})$ and RPS obtained from the five repetitions at each given source–detector fibre pair were used in the reconstruction vector \mathbf{z} , and are hereafter simply referred to as the *measurements*. The measurements obtained for both the experimental cases employing both the referencing schemes were compared to the simulated data obtained from the forward model (see figure 4 for imperfect uptake case). The difference between the measurements and simulated data is thus an assessment of what was termed as *model error*. In addition to errors introduced by the computational forward model itself (e.g., discretization error, simplifications in the physics, errors in parameters and boundary conditions considered known, etc), here the definition of model error also includes any biased portion of the measurement error.

3.1.1. Model error using first (dual-wavelength) referencing scheme. Model predictions poorly matched measurements when the excitation wavelength based referencing scheme (equation (2)) was used for both the perfect and imperfect experimental data. A comparison plot of $\ln(\text{ACR})$ and RPS between measurements and predictions from the forward model (for the imperfect uptake case) is shown in figures 4(a) and (b), respectively. Similar mismatch in both the parameters $\ln(\text{ACR})$ and RPS) was observed for the perfect uptake experimental case as well. The predictions of both $\ln(\text{ACR})$ and RPS were highly biased (i.e. mean model error was far from zero) for both sets of experimental data. In addition, the absolute scale of RPS predictions was lower than that of the actual measurements, resulting in high model error variance for RPS. These large errors are believed to occur due to the

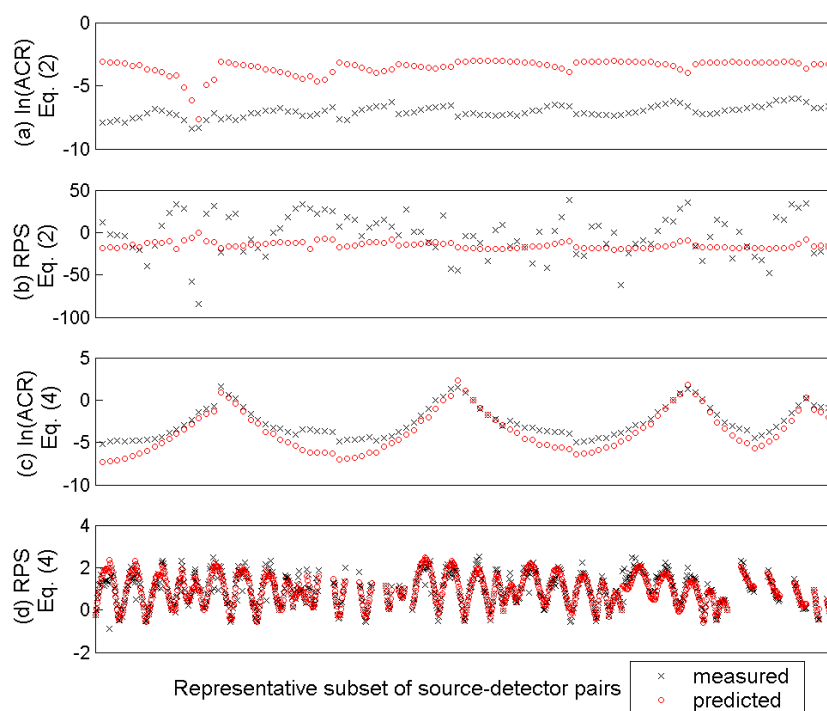


Figure 4. Comparison of model predictions with measurements for $\ln(\text{ACR})$ and RPS, shown for a representative subset of source–detector pairs in the imperfect uptake case, using first (equation (2)) referencing scheme (a), (b) and second (equation (4)) referencing scheme (c), (d).

unaccountable wavelength dependence of the image intensifier under the current operating conditions. The characteristics of the image intensifier provided by the manufacturer were insufficient to accurately characterize the wavelength dependence of the image intensifier over the voltage ranges it was operated at. Hence, no good match was obtained between measurements and forward model predictions when the referencing method in equation (2) was used.

3.1.2. Model error using second referencing scheme. Upon employing the second referencing scheme utilizing designated reference detectors at the emission wavelength (equation (4)), a better match between model predictions and observed measurements was observed for both the experimental datasets (see figures 4(c) and (d) for comparison plots of imperfect uptake case). Similar model match in terms of $\ln(\text{ACR})$ and RPS was observed for the perfect uptake case as well. The histograms of the model error for the two experiments given in figure 5 show that the RPS exhibited relatively low bias and variance. Model error for $\ln(\text{ACR})$ showed higher bias and variance than RPS (figures 4(c), (d) and 5), but was much less biased than that observed when referencing to excitation light (i.e. using the first referencing scheme) (figure 4(a)). Model error variance was observed to increase sharply for measurements with modulation depth <0.025 . The relatively high model errors in $\ln(\text{ACR})$ could possibly be due to an image retention effect in the image intensifier of the ICCD system that tends to affect the ac amplitude but not the phase. An additional source of potential bias in the error for both $\ln(\text{ACR})$ and RPS may arise from the assumption that the lengths of all the

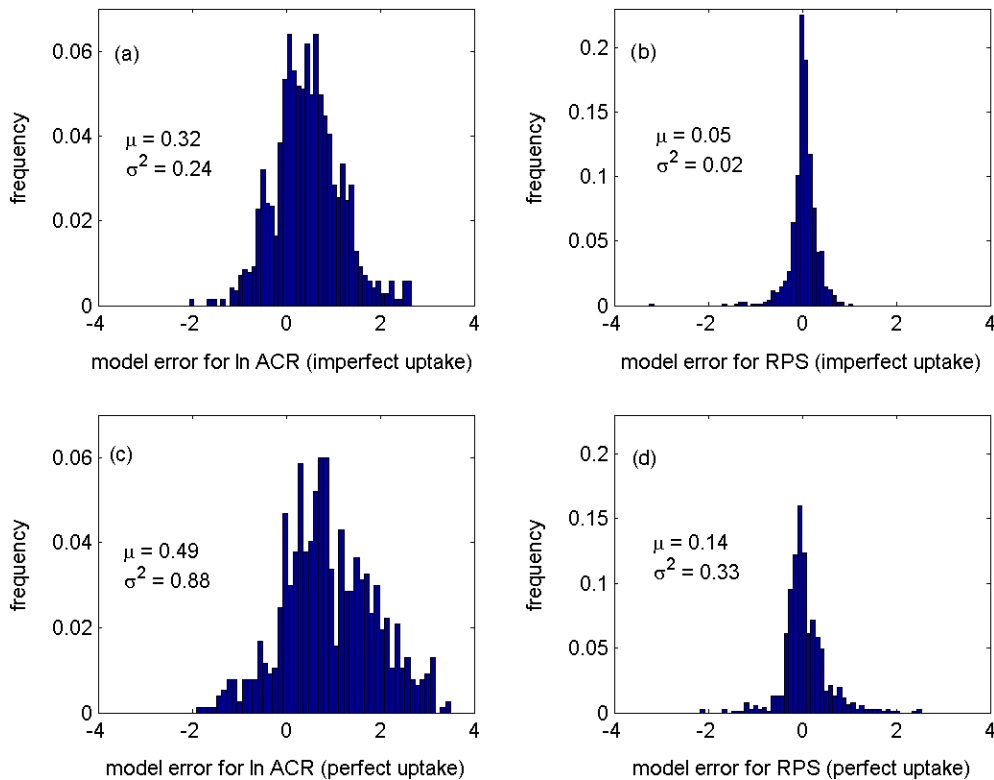


Figure 5. Histograms of model error for the two experiments, using the referencing method shown in equation (4), for (a) ln(ACR), imperfect uptake, (b) RPS, imperfect uptake, (c) ln(ACR), perfect uptake, (d) RPS, perfect uptake.

collection fibres are identical. However, the actual lengths in the current experimental set-up varied to a small extent.

If accurate determination of the wavelength dependence of the image intensifier becomes available, the first referencing method may ultimately prove to be the method of choice as observed by other researchers (Lee and Sevick-Muraca 2002, Roy *et al* 2003). However, because of the relatively unbiased model error and highly reduced model error variance for RPS using the second referencing method relative to the first referencing method, reconstructions were performed using the referenced data from the second scheme.

3.2. Measurement error

Measurement error variances (used on the diagonal of \mathbf{R}) were calculated for each source–detector pair as $s^2/5$, where s is the sample standard deviation of the five repetitions from each source–detector pair, using the second referencing method. The average measurement error variance for both ln(ACR) and RPS under both the experimental conditions are given in figure 6. It should be noted that the current assessment of measurement error does not include possible bias in measurement errors, and the biased portion was considered as a component of the model error.

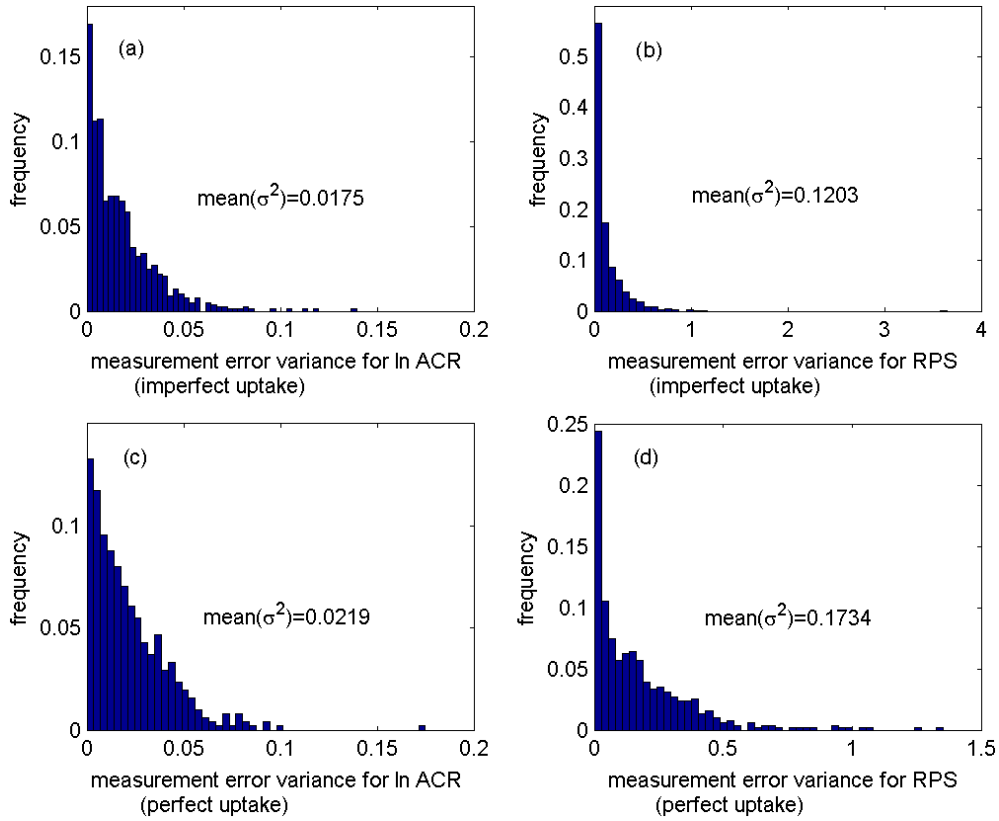


Figure 6. Histograms of measurement error variances for all measurements (referenced as shown in equation (4) with modulation depth >0.025 for (a) $\ln(\text{ACR})$, imperfect uptake, (b) RPS, imperfect uptake, (c) $\ln(\text{ACR})$, perfect uptake, (d) RPS, perfect uptake.

3.3. Image reconstructions

For image reconstructions, individual referenced measurements with modulation depth <0.025 were neglected, in order to minimize the propagation of errors into the inversion scheme while speeding up the reconstructions. This reduced the datasets to a total of 429 emission measurements for the imperfect uptake case and 207 emission measurements for the perfect uptake case. These referenced measurements (using the second referencing method) were used along with the estimates of measurement error covariance \mathbf{R} and model error covariance \mathbf{Q} in order to reconstruct the 3D optical property map of μ_{axf} using the inversion algorithm described in section 2.6. Low and spatially variable signal to noise ratios (SNR) in fluorescence emission data were thus accommodated by filtering out low SNR data at three levels, as follows: (i) source level: point source locations were limited to those which elicit an average modulation depth greater than 0.1 for each interfacing plate (section 2.3), (ii) detector level: only those detected emission measurements with individual modulation depth greater than 0.025 were used in the inversion and (iii) update level: parameter updates were weighted in a spatially variant manner based on the observed variance and inverse modulation depth of each measurement (section 2.6). For both the experimental datasets, μ_{axf} was initially assumed homogeneous with low absorption coefficient of 0.003 cm^{-1} .

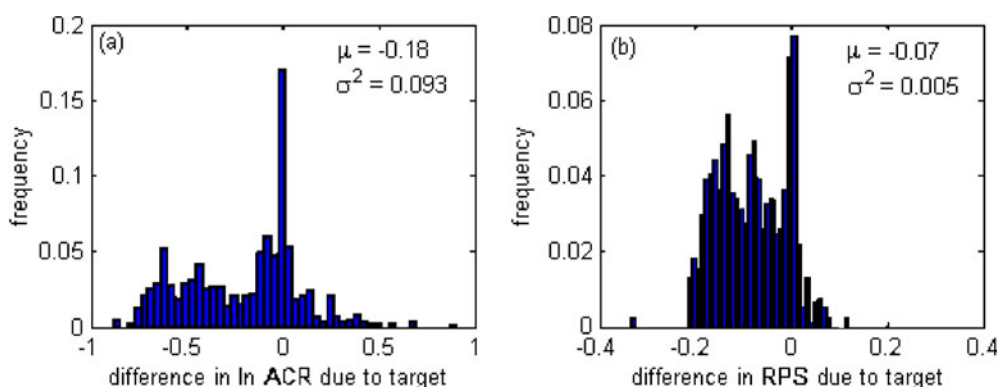


Figure 7. Histograms of differences in model predictions with and without the fluorescent target, assuming background fluorescence absorption of 0.003 cm^{-1} , for (a) $\ln(\text{ACR})$, (b) RPS.

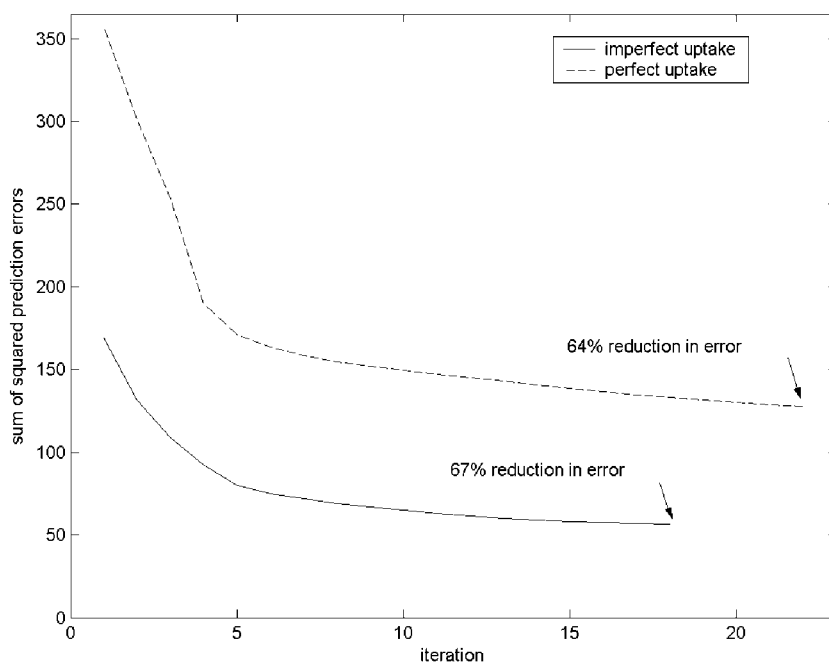


Figure 8. Convergence curves of sum of squared prediction errors for the two reconstructions.

Histograms of the differences in signal between model predictions with and without the fluorescent target are shown in figure 7, and are a measure of the signal information available for reconstruction of the target. Comparing these frequency distributions of the signal change due to the heterogeneity with those obtained for model error (figure 5) and measurement error (figure 6), it is apparent that the SNR is low for both datasets. Nonetheless, both reconstructions converged smoothly (figure 8). The target location was identifiable after the first iteration (4–7 min) and the inversions converged (exhibited less than a 1% decrease in model prediction error) after 22 iterations (1.4 h) and 18 iterations (2 h), for the imperfect and perfect uptake cases, respectively, on a 2.2 GHz Pentium IV. The isosurfaces at 0.2 cm^{-1} for 3D phantom containing the actual target (i.e. the known target in the actual experimental set-up), for the

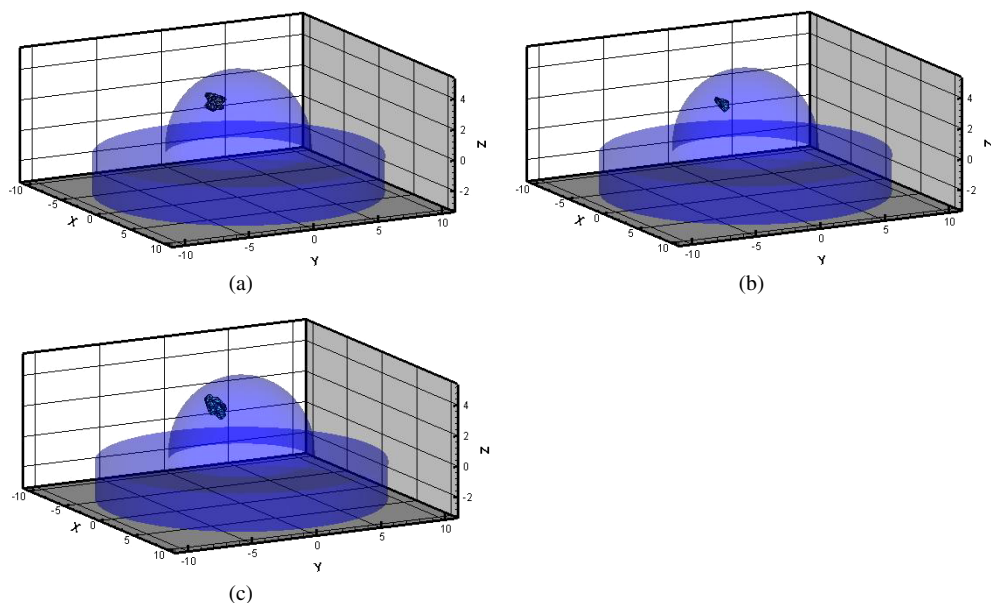


Figure 9. (a) The true fluorescence absorption distribution in the 3D phantom containing the actual target. In both experiments, the value of the absorption coefficient due to fluorophore (μ_{axf}) in the actual target was 0.30 cm^{-1} . The background μ_{axf} value was 0.003 cm^{-1} and 0.000 cm^{-1} in the imperfect and perfect uptake case, respectively. (b) The fluorescence absorption distribution in the 3D reconstructed phantom for the imperfect uptake case, with isosurface shown at $\mu_{\text{axf}} = 0.2 \text{ cm}^{-1}$. (c) The fluorescence absorption distribution in the 3D reconstructed phantom for the perfect uptake case, with isosurface shown at $\mu_{\text{axf}} = 0.2 \text{ cm}^{-1}$.

M An AVI movie of this figure is available from stacks.iop.org/PMB/48/1701

3D reconstructed phantom in the imperfect uptake case and the 3D reconstructed phantom in the perfect uptake case are plotted in figures 9(a), (b) and (c), respectively. The figures are 3D plots of the absorption coefficient due to the fluorophore (μ_{axf}) in the breast phantom, where isosurface cut-off value was set to $\mu_{\text{axf}} = 0.2 \text{ cm}^{-1}$, in order to discriminate the region of interest (i.e., the target in this case) from the background. All nodes with estimates above the arbitrary cut-off of $\mu_{\text{axf}} > 0.2 \text{ cm}^{-1}$ were considered elevated. These nodes were then spatially clustered into distinct heterogeneities and each heterogeneity was characterized by volume-integrated fluorescence absorption (volume-weighted averages of nodal μ_{axf} within each identified heterogeneity), value-weighted centroid locations and Euclidean distance of the identified centroid from the location of the true centroid of the target. A single target was identified in both the imperfect and perfect uptake reconstructions (figures 9(b) and c), located only 0.52 cm and 0.32 cm , respectively, away from the actual target location. These reconstructions are quantified in table 3 for completeness. The target volumes were underestimated in both cases, although this value is dependent on the arbitrarily chosen isosurface value that defines the target boundary. The quantitative estimate of integrated fluorescence absorption was underestimated in the imperfect case, and overestimated in the perfect uptake case (table 3). Choice of specific reference nodes affected the quantitative results and presence or absence of artefacts, although the target was consistently identified.

The discrepancies between the actual target (in terms of size and location) and the reconstructed targets in both the experimental cases could possibly be due to (i) sparse and

Table 3. Centroid locations and integrated values of areas where fluorescence absorption (μ_{axf}) was greater than 0.2 cm^{-1} .

Experiment	Heterogeneity	Centroid x (cm)	Centroid y (cm)	Centroid z (cm)	Distance off (cm)	Integrated μ_{axf} (cm^{-1})	Volume (cm^3)
Known phantom	Actual target	-2.50	-0.50	2.50	–	0.30	1.00
Imperfect uptake	Identified target	-2.04	-0.74	2.45	0.52	0.14	0.38
Perfect uptake	Identified target	-2.30	-0.73	2.60	0.32	0.43	0.69

noisy experimental data, (ii) measurement and model errors due to the experimental set-up and discretization of the phantom mesh, respectively, (iii) experimental error in terms of positioning the target at the specified location and/or (iv) non-optimal choices for control variables in the inversion, such as initial parameter variance.

4. Conclusions

A novel fluorescence-enhanced FDPM imaging system was developed using an ICCD camera for rapid data acquisitions. Initial experiments performed using large breast-shaped tissue-mimicking phantoms exhibited a much better model match with a finite element implementation of the coupled diffusion equations when emission measurements were referenced to specified detectors at the emission wavelength rather than when they were referenced to excitation measurements at each detector location. Despite the low and spatially variable signal to noise ratio (SNR), the 1 cm^3 fluorescent target containing $1 \mu\text{M}$ ICG was identified in the correct location in the 3D reconstructions of fluorescence absorption for both imperfect (100 : 1) and perfect uptake (1 : 0) cases, although the estimates were not quantitatively accurate.

Extensive work will be carried out in order to determine the performance and limitations of the developing imaging system before it can be clinically applicable. Future experiments using the existing prototype imaging system will involve data acquisition and reconstructions using single and multiple targets at various depths, volumes and levels of fluorescent contrast, in order to assess the robustness of the ICCD imager before executing modifications to the imaging set-up. Lifetime studies will also be performed by exploiting the advantages of a frequency-domain imaging system over a CW system, where the enhanced phase contrast due to the differences in lifetime between the target and the background can be measured. Although it is encouraging that useful images can be reconstructed with low SNR, greater improvements in the data acquisition technology will be needed to further reduce the noise level. Replacing the fibre optic detectors and interfacing plates with a single optical fibre bundle, similar to those used in endoscopic procedures, would not only reduce measurement errors, but would also make the imager more compact and robust. Improvements in meshing schemes may enable reductions in discretization error in the forward model. Better estimates of initial parameter error, measurement error and model error covariances (**P**, **R** and **Q**, respectively) may improve the quantitative accuracy of the inversions.

Acknowledgment

The research was supported by National Institutes of Health (NIH R01CA88082).

References

- Chang J, Barbour R L, Graber H and Aronson R 1995 Fluorescence optical tomography *Proc. SPIE* **2570** 59–72
- Chang J, Graber H L and Barbour R L 1997 Imaging of fluorescence in highly scattering media *IEEE Trans. Biomed. Eng.* **44** 810–22
- Chang J, Graber H L and Barbour R L 1998 Improved reconstruction algorithm for luminescence when background luminophore is present *Appl. Opt.* **37** 3547–52
- Chernomordik V, Hattery D, Gannot I and Gandjbakhche A H 1999 Inverse method 3-D reconstruction of localized *in vivo* fluorescence—application to Sjogren syndrome *IEEE J. Sel. Top. Quantum Electron.* **54** 930–5
- Delpy D T and Cope M 1997 Quantification in tissue near-infrared spectroscopy *Phil. Trans. R. Soc. B* **352** 649–59
- Eppstein M J and Dougherty D E 1996 Simultaneous estimation of transmissivity values and zonation *Water Resour. Res.* **32** 3321–36
- Eppstein M J, Dougherty D E, Hawrysz D J and Sevick-Muraca E M 1999a Three-dimensional optical tomography *Proc. SPIE* **3497** 97–105
- Eppstein M J, Dougherty D E, Troy T L and Sevick-Muraca E M 1999b Biomedical optical tomography using dynamic parameterization and Bayesian conditioning on photon migration measurements *Appl. Opt.* **38** 2138–50
- Eppstein M J, Hawrysz D J, Godavarty A and Sevick-Muraca E M 2002 Three-dimensional, near-infrared fluorescence tomography with Bayesian methodologies for image reconstruction from sparse and noisy data sets *Proc. Natl. Acad. Sci. USA* **99** 9619–24
- Fedele F, Laible J P and Eppstein M J 2003 Coupled complex adjoint sensitivities for frequency-domain fluorescence tomography: theory and vectorized implementation *J. Comput. Phys.* **187** 597–619
- Godavarty A, Hawrysz D J, Roy R, Sevick-Muraca E M and Eppstein M J 2002 The influence of the refractive index-mismatch at the boundaries measured in fluorescence-enhanced frequency-domain photon migration imaging *Opt. Exp.* **10** 653–62
- Gurfinkel M *et al* 2000 Pharmacokinetics of ICG and HPPH-car for the detection of normal and tumor tissue using fluorescence, near-infrared reflectance imaging: a case study *Photochem. Photobiol.* **72** 94–102
- Haskell R C *et al* 1994 Boundary conditions for the diffusion equation in radiative transfer *J. Opt. Soc. Am. A* **11** 2727–41
- Hawrysz D J, Eppstein M J, Lee J and Sevick-Muraca E M 2001 Error consideration in contrast-enhanced three-dimensional optical tomography *Opt. Lett.* **26** 704–6
- Hebden J C, Veenstra H, Dehghani H, Hillman E M C, Schweiger M, Arridge S R and Delpy D T 2001 Three-dimensional time-resolved optical tomography of a conical breast phantom *Appl. Opt.* **40** 3278–87
- Houston J P, Thompson A B, Gurfinkel M and Sevick-Muraca E M 2003 Sensitivity and depth penetration of continuous wave versus frequency-domain photon migration near-infrared fluorescence contrast-enhanced imaging *Photochem. Photobiol.* **77** 420–30
- Hull E L, Nichols M G and Foster T H 1998 Localization of luminescent inhomogeneities in turbid media with spatially resolved measurements of cw diffuse luminescence emittance *Appl. Opt.* **37** 2755–65
- Jiang H 1998 Frequency-domain fluorescent diffusion tomography: a finite-element-based algorithm and simulations *Appl. Opt.* **37** 5337–43
- Lakowicz J R and Berndt K W 1991 Lifetime-selective fluorescence imaging using an rf phase-sensitive camera *Rev. Sci. Instrum.* **62** 1727–34
- Lee J and Sevick-Muraca E M 2002 3-D fluorescence enhanced optical tomography using referenced frequency-domain photon migration measurements at emission and excitation measurements *J. Opt. Soc. Am. A* **19** 759–71
- Ntziachristos V and Weissleder R 2001 Experimental three-dimensional fluorescence reconstruction of diffuse media by use of a normalized Born approximation *Opt. Lett.* **26** 893–5
- Ntziachristos V and Weissleder R 2002 Charge-coupled-device based scanner for tomography of fluorescent near-infrared probes in turbid media *Med. Phys.* **29** 803–9
- O’Leary M A, Boas D A, Chance B and Yodh A G 1994 Reradiation and imaging of diffuse photon density waves using fluorescent inhomogeneities *J. Luminescence* **60**, **61** 281–6
- O’Leary M A, Boas D A, Li X D, Chance B and Yodh A G 1996 Fluorescence lifetime imaging in turbid media *Opt. Lett.* **21** 158–60
- Paithankar D Y, Chen A U, Pogue B W, Patterson M S and Sevick-Muraca E M 1997 Imaging of fluorescent yield and lifetime from multiply scattered light reemitted from random media *Appl. Opt.* **36** 2260–72
- Reddy J N 1993 *An Introduction To The Finite Element Method* 2nd edn (New York: McGraw-Hill)
- Reynolds J S, Troy T L, Mayer R H, Thompson A B, Waters K K, Cornell D J, Snyder P W and Sevick-Muraca E M 1999 Imaging of spontaneous canine mammary tumors using fluorescent contrast agents *Photochem. Photobiol.* **70** 87–94

- Reynolds J S, Troy T L and Sevick-Muraca E M 1997 Multipixel techniques for frequency-domain photon migration imaging *Biotechnol. Prog.* **13** 669–80
- Roy R, Godavarty A and Sevick-Muraca E M 2003 Fluorescence-enhanced, optical tomography using referenced measurements of heterogeneous media *IEEE Trans. Med. Imaging* at press
- Roy R and Sevick-Muraca E M 1999 Truncated Newton's optimization scheme for absorption and fluorescence optical tomography: Part II Reconstruction from synthetic measurements *Opt. Exp.* **4** 372–82
- Roy R and Sevick-Muraca E M 2000 Active constrained truncated Newton method for simple-bound optical tomography *J. Opt. Soc. Am. A* **17** 1627–41
- Roy R and Sevick-Muraca E M 2001a Three-dimensional unconstrained and constrained image-reconstruction techniques applied to fluorescence, frequency-domain photon migration *Appl. Opt.* **40** 2206–15
- Roy R and Sevick-Muraca E M 2001b A numerical study of gradient-based nonlinear optimization methods for contrast-enhanced optical tomography *Opt. Exp.* **9** 49–65
- Sevick-Muraca E M, Godavarty A, Houston J P, Thompson A B and Roy R 2003 Near-infrared imaging with fluorescent contrast agents *Handbook of Biomedical Fluorescence* ed B W Pogue and M-A Mycek (New York: Marcel Dekker Inc.) pp 445–527
- Sun Z, Huang Y and Sevick-Muraca E M 2002 Precise analysis of frequency domain migration measurement for characterization of concentrated colloidal suspensions *Rev. Sci. Instrum.* **73** 383–93
- Thompson A B, Hawrysz D J and Sevick-Muraca E M 2003 Near-infrared fluorescence contrast-enhanced imaging with area illumination and area detection: the forward imaging problem *Appl. Opt.* at press
- Thompson A B and Sevick-Muraca E M 2003 Near-infrared fluorescence contrast-enhanced imaging with intensified charge-coupled device homodyne detection: measurement precision and accuracy *J. Biomed. Opt.* **8** 111–20
- Wu J, Perelman L, Dasari R R and Feld M S 1997 Fluorescence tomographic imaging in turbid media using early-arriving photons and Laplace transforms *Proc. Natl. Acad. Sci.* **94** 8783–8
- Wu J, Wang Y, Perelman L, Itzkan I, Dasari R R and Feld M S 1995 Time-resolved multichannel imaging of fluorescent objects embedded in turbid media *Opt. Lett.* **20** 489–91
- Yang Y, Iftimia N, Xu Y and Jiang H 2001 Frequency-domain fluorescent diffusion tomography of turbid media and *in vivo* tissues *Optical Tomography and Spectroscopy of Tissue IV (San Jose, CA)* *Proc SPIE* **4250** 537–45
- Zhang C, Eppstein M J, Godavarty A and Sevick-Muraca E M 2003 A hybrid approach to Bayesian image reconstruction *Proc SPIE* **4955** at press
- Zeinkiewicz O C and Taylor R L 1989 *The Finite Element Methods In Engineering Science* (New York: McGraw-Hill)